nature communications

Article

https://doi.org/10.1038/s41467-025-59670-w

Elastic circular organic microcrystals prepared by photoinduced delamination

Received: 29 December 2024

Accepted: 30 April 2025

Published online: 28 May 2025

Check for updates

Chengde Ding[1], Baolei Tang[1], Liang Li[2,3], Panče Naumov[2,4,5,6] ✉ & Hongyu Zhang[1] ✉

Circular organic crystals are essential as optically transducive components in flexible organic optoelectronics, yet this crystal habit is not easily obtained through traditional crystallization approaches. Here, we present a photoresponsive organic crystalline material that when exposed to ultraviolet or visible light, initially undergoes photoinduced bending, followed by photosalient effect and accompanied by delamination to elastic quasicircular microcrystals. Curvature analysis under different conditions confirms the controllability of this process. Light at 365 nm, 405 nm, and 445 nm generates microcrystals with high curvatures (11–12 mm^{-1}), while 470 nm light produces lower curvature (5 mm^{-1}), aligning with the absorption profile. Increasing the excitation power from 15 mW to 150 mW results in increase of the yield of microcrystals with high curvatures (10–20 mm^{-1}) from 20% to 94%. This light-driven fabrication method provides a controlled and reproducible means of realizing rare crystal morphologies, highlighting the potential for exploring quantitative relationships between such morphologies and their unconventional optical properties.

In modern materials science, precise control over the shape and functionality of materials is crucial[1–3], especially for the development of smart materials and advanced devices[4–7]. Accurate regulation of morphology and properties not only broadens the diversity and adaptability of the materials, but it also is required to address challenges with both contemporary and future applications[8–12], with potential to foster innovations in emerging domains such as biomedical devices, flexible electronics, and sensors[13–15]. Against this backdrop, ring-shaped material architectures have emerged as a recurring, yet uncommon motif explored in natural sciences, owing to their high symmetry, mechanical stability, and adaptability in shape[16–18]. At a molecular scale, cyclic molecules such as crown ethers[19,20] and cyclodextrins[21] are established well in chemical synthesis, catalysis, and supramolecular recognition processes. At the nanolevel, cyclic nanostructures, such as carbon nanorings, exhibit exceptional optoelectronic properties due to their symmetry and structure[22]. At a microscale, circular structures are exemplified by microring resonators[23], a class of optical devices that leverage the circular pathways of light for efficient filtering and signal transmission in optical communication and photonic integrated circuits[24]. These examples, which represent only a small subset of the plethora of available circular architectures, highlight the importance of ring-shaped structures in achieving stability, efficiency, and adaptability.

A photomechanical deformation refers to reshaping of an object that is induced or assisted by light, and it offers a non-contact method for controlling the morphology and functionality of the material[25–32]. This mechanism of shape manipulation has been demonstrated with bending[2,33–42], curling[43–46], twisting[31,47–52], and delamination[53–56], and has been applied to control both macroscopic shapes and microstructural configurations. For example, by modulating the bending and

[1]State Key Laboratory of Supramolecular Structure and Materials, College of Chemistry, Jilin University, Changchun 130012, P. R. China. [2]Smart Materials Lab, New York University Abu Dhabi, Abu Dhabi, UAE. [3]SAFIR Novel Materials Development Lab, Sorbonne University Abu Dhabi, Abu Dhabi, UAE. [4]Center for Smart Engineering Materials, New York University Abu Dhabi, Abu Dhabi, UAE. [5]Research Center for Environment and Materials, Macedonian Academy of Sciences and Arts, Bul. Krste Misirkov 2, Skopje, Macedonia. [6]Molecular Design Institute, Department of Chemistry, New York University, 100 Washington Square East, New York, NY, USA. ✉e-mail: pance.naumov@nyu.edu; hongyuzhang@jlu.edu.cn

deformation of flexible crystals under illumination, applications such as soft robotic grippers or artificial bioinspired actuator replicas become feasible[29,57,58]. Among these mechanisms, studies on photo-induced delamination in organic crystals remain relatively limited, despite that this post-processing of crystals could hold significant importance as it results in unconventional shapes that are not always available via the most commonly used method, crystallization. The delaminated crystals, if sufficiently thin, often form curled structures during delamination, however they usually do not curl sufficiently to close a complete circle. Consequently, the controlled and scalable preparation of flexible organic ring-shaped crystals remains a significant and unresolved challenge. In this context, we address this challenge by reporting a flexible organic crystal, **MBID**, that undergoes photoinduced delamination to form ring-shaped microcrystals under light stimulation. Unlike conventional brittle organic crystals, **MBID** exhibits exceptional flexibility and a propensity for photoinduced delamination, resulting in microcrystals with quasicircular habits. We investigate the factors influencing the delamination process and elucidate the underlying mechanisms through crystal structure analysis. This work not only provides a scalable and controllable method for fabricating ring-shaped organic crystals but also highlights the broader implications of photomechanical post-processing for advancing functional materials.

Results and discussion

Preparation and characterization

The material, 2-(4-(methylthio)benzylidene)-1*H*-indene-1,3(2*H*)-dione (**MBID**; Fig. 1a) was synthesized with an 84% yield via Knoevenagel condensation reaction between 1*H*-indene-1,3(2*H*)-dione and 4-(methylthio)benzaldehyde. The identity of the product was confirmed with proton and carbon nuclear magnetic resonance (NMR) spectroscopy (Supplementary Figs. 1, 3), as well as with single-crystal X-ray diffraction (SCXRD) analysis (Supplementary Table 1). Yellow crystals were obtained by layering ethanol over a dichloromethane solution of **MBID**, allowing for gradual solvent diffusion at room temperature (Fig. 1b). The crystals are thermally stable, with melting points ranging from 418 K to 432 K, and exhibit no phase transition upon heating from room temperature to 418 K (Supplementary Fig. 4). In dichloromethane solution (10^{-5} M), **MBID** appears yellow under daylight due to the absorption with a maximum at 410 nm, and emits faint green fluorescence under 365 nm (UV) light with an emission band around 481 nm (Supplementary Fig. 5). Crystalline **MBID** shows maximum absorption at 337 nm that extends over 400 nm, and emits bright green fluorescence with a maximum emission wavelength of 527 nm (Fig. 1b, c). The crystals exhibit excellent elasticity, and can undergo repeated and reversible bending under external force field without visible damage (Fig. 1d). To assess the mechanical properties of the crystals, we performed tensile measurements, which determined their average tensile modulus at 298 K to be 0.12 GPa (Fig. 1e). We noticed that during the exposure to ultraviolet or visible light, the **MBID** crystals exhibit an unusual photoinduced delamination, resulting in the formation of distinct curved microcrystals with varying curvatures (Fig. 1f), as well as strongly curled crystals. In the latter case, the termini partially overlap with each other, forming a quasicircular shape (Fig. 1h). Both types of microcrystals obtained through delamination demonstrate excellent elasticity. The arc-shaped microcrystals can be repeatedly bent several times without damage (Figs. 1g, and Supplementary Movies 1, 2), while the quasicircular microcrystals can be distorted from circular to elliptical geometry by compression, and return to their original form once the external force has been removed (Fig. 1i, and Supplementary Movies 3–5). Given the unusual appearance and favorable elasticity of the microcrystals, we posit that this combination of shape and mechanical properties could be relevant to flexible electronic devices, deformable electronic systems, and micromechanical systems, similar to the prospects for other flexible crystals.

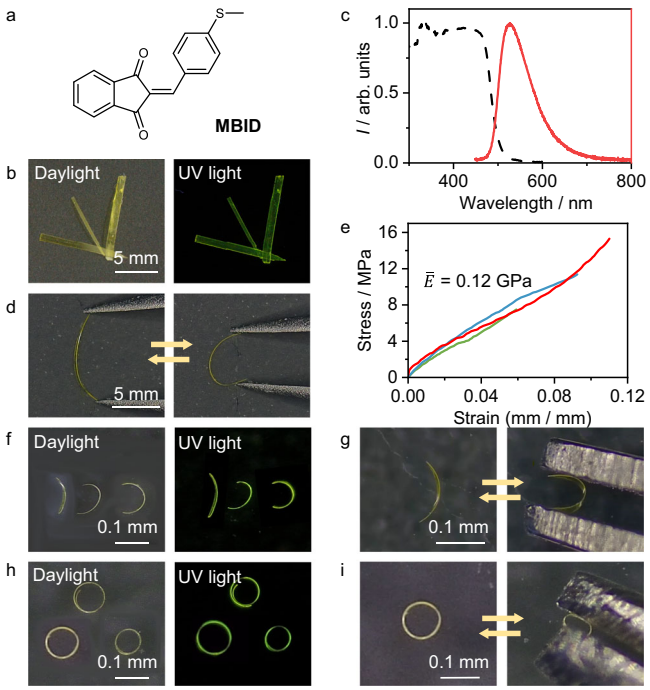

Fig. 1 | Structure, appearance and properties of MBID. a Chemical structure of **MBID**. **b** Photographic images of **MBID** crystals under daylight and UV light. **c** UV-vis absorption (broken line) and emission (solid line) spectra of **MBID** crystals. **d** Reversible bending and unbending of a thin, long **MBID** crystal. **e** Stress-strain curves of three **MBID** crystals. **f**, **h** Photographic images of arc-shaped (**f**) and ring-shaped (**h**) microcrystals recorded under daylight and UV light. **g**, **i** Reversible bending and unbending experiments of arc-shaped (**g**) and ring-shaped (**i**) microcrystals. (Source data are provided as a Source Data file).

Photomechanical behavior of MBID crystals

Considering that the chemical structure of **MBID** includes double bonds and is nearly planar, similar to other photoresponsive crystals[3], we anticipated that such crystals are likely to be photomechanically active. Indeed, when irradiated with UV light **MBID** crystals show an unusual, complex photomechanical motion (Fig. 2a and Supplementary Movie 6). In the first 20 s, the crystals quickly bend towards the light source. With continued exposure, the bending angle increases further, although the rate of bending slows down. After 80 s of exposure, the crystals begin to delaminate, accompanied by brief but intense vibrations and evolution of cracks. Following the delamination, the bending angle notably decreases, likely due to significant release of the accumulated intramolecular strain, highlighting its mechanical resilience[2]. This photomechanical effect also occurs when the crystal is exposed to visible light (Supplementary Movie 7). This series of photomechanical effects can be summarized as photochemical bending, which, after reaching a certain threshold, causes the crystal to suddenly vibrate and crack—similar to a phenomenon known as photosalience[59]. Simultaneously, the crystal undergoes light-induced delamination, where we believe the photosalience and delamination occur simultaneously. Upon closer inspection at higher magnification, we found that the photoinduced delamination is distinct among the similar photomechanical materials (Fig. 2b). Unlike other crystals capable of photodelamination, after the delamination the crystal of **MBID** has arc-shaped crystalline fragments and peculiar ring-shaped microcrystals on its surface. Some of these microcrystals spontaneously detach from the crystal surface, while others remain attached.

We hypothesized that this distinct delamination behavior holds potential as an alternative method for preparation of arc-shaped and

https://doi.org/10.1038/s41467-025-59670-w

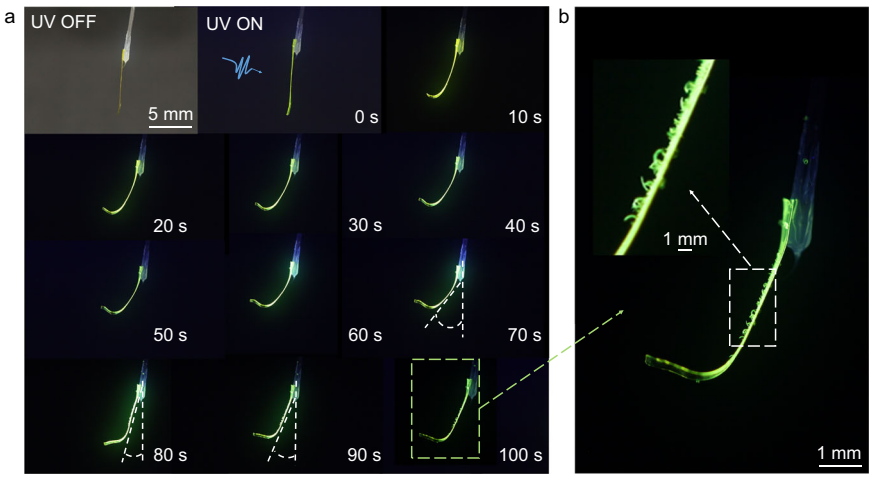

Fig. 2 | Photomechanical effects and delamination of MBID. a Photoinduced bending and delamination of a crystal that has been fixed onto a pin and exposed to UV light. **b** Zoomed-in images showing the quasicircular crystals evolving from the surface of the irradiated crystal at the time point corresponding to 100 s from the irradiation onset.

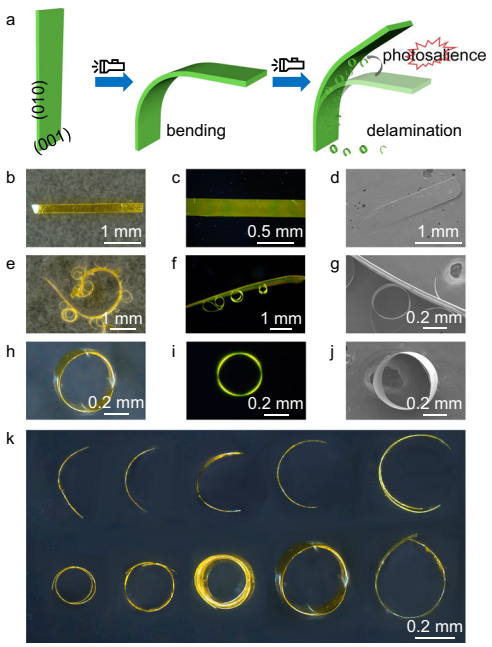

Fig. 3 | Formation, size and shape of the curved and quasicircular MBID crystals. a Schematics illustrating the photomechanical effects of the parent crystals. **b**–**d** Non-polarized optical (**b**), polarized optical (**c**), and scanning electron (**d**) images of the parent crystal. **e**–**g** Non-polarized optical (**e**), polarized optical (**f**), and scanning electron (**g**) images of the crystal after irradiation with 365 nm UV light, showing delamination on its surface. **h**–**j** Non-polarized optical (**h**), polarized optical (**i**), and scanning electron (**j**) images of a ring-shaped microcrystals obtained by delamination. **k** Optical micrographs of arc-shaped microcrystals with different curvatures (top) and quasicircular microcrystals with different radii (bottom) obtained from the parent crystal.

ring-shaped microcrystals. The process is rationalized with the schematic illustration in Fig. 3a, based on face indexing of the crystals (Supplementary Fig. 6). When the (001) facet of the crystal is illuminated, it bends towards the light source. Prolonged illumination induces photosalient effect and photoinduced delamination, leading to the formation of arc-shaped and ring-shaped microcrystals, which either remain attached to the original crystal surface or completely separate from it. Using optical microscopy, polarized light microscopy, and scanning electron microscopy (SEM), we examined the morphology of the crystals before and after the photoinduced delamination, as well as the morphology of the ring-shaped microcrystals. Prior to illumination, the crystal surface was smooth and flat with no visible cracks (Fig. 3b, d and Supplementary Fig. 7a), and was birefringent under polarized light (Fig. 3c). During illumination, the crystal gradually bent and delaminated. When observed along the [010] direction, the arc-shaped and ring-shaped microcrystals were clearly visible when they were either attached to or detached from the crystal surface (Fig. 3e–g and Supplementary Fig. 7b–d). The ring-shaped microcrystals formed by delamination exhibited stable and uniform geometries with smooth surfaces free of cracks and retained their birefringence (Fig. 3h, i). SEM revealed that the ring-shaped crystals did not form fully closed loops; instead, due to significant curling or bending, their ends overlapped, forming an end-to-end-connected circular structures (Fig. 3j and Supplementary Fig. 7e, f).

Controllable preparation and curvature modulation of quasicircular crystals

All the microcrystals generated by photoinduced delamination displayed excellent mechanical elasticity. Although this characteristic suggests potential applications in flexible optoelectronic devices or micromechanical systems, actual implementation would require control over the morphology and size of such crystals. To investigate this possibility, we fabricated a series of arc-shaped and ring-shaped microcrystals of varying curvatures (Fig. 3k). These microcrystals exhibited diverse morphological features: the radii of the arc-shaped crystals ranged from tens to hundreds of micrometers, while the ring-shaped crystals formed structures with different radii. Although the crystals had round shapes, they were not perfectly circular and displayed slightly asymmetrical features. This asymmetry may result from slight thickness variations in different regions of the **MBID** crystals or uneven light exposure, which could lead to non-uniform stress distribution during the photoinduced delamination process, reflecting the complexity of the photochemical, morphological, and structural effects that account for the observed delamination and curling. Consequently, statistical analysis was conducted on the curvature of arc-shaped and ring-shaped microcrystals prepared by delamination under various conditions to assess the controllability of the process. Crystals were irradiated with light of different wavelengths (Fig. 4a and Supplementary Table 2). The power at all wavelengths (365 nm, 405 nm, 445 nm, 470 nm, and 515 nm) was 100 mW, and the light exposure time lasted until the **MBID** crystals started to delaminate. The results showed that when illuminated at 365 nm, 405 nm, and

https://doi.org/10.1038/s41467-025-59670-w

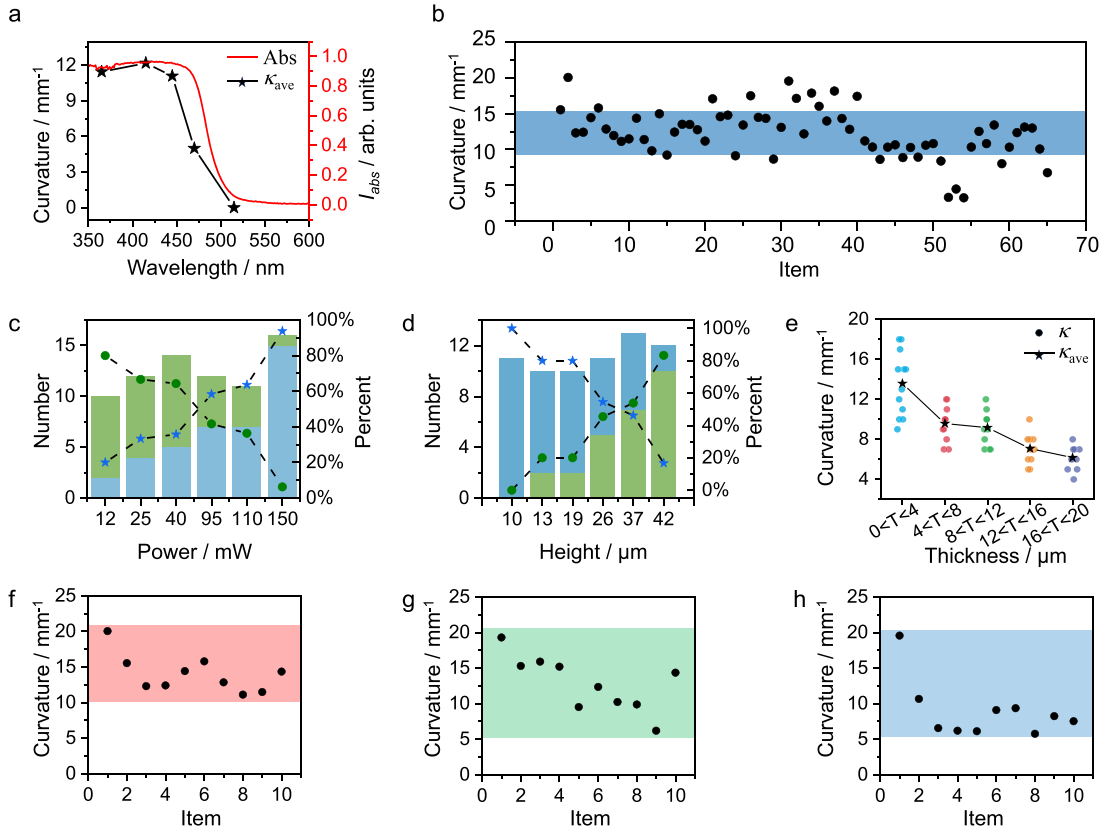

Fig. 4 | Factors that determine the curvature of the quasicircular crystals. **a** Mean curvature of the delaminated microcrystals at different illumination wavelengths (black line) and UV-vis absorption spectrum (red line) of **MBID** crystals. **b** Experimentally determined curvatures (κ) for 65 quasicircular microcrystals (the x axis corresponds to the sample number). **c**–**e** Dependence of the curvature on the illumination power ($0 < \kappa < 10$ mm^{-1}: green bars and symbols, $10 < \kappa < 20$ mm^{-1}: blue bars and symbols) (**c**), height (thickness) of the parent crystal ($0 < \kappa < 10$ mm^{-1}: green bars and symbols, $10 < \kappa < 20$ mm^{-1}: blue bars and symbols) (**d**), and thickness (T) of the microcrystal (**e**). **f**–**h** Experimentally determined curvatures of crystals irradiated for 0 s (**f**), 10 s (**g**), and 20 s (**h**) with a 405 nm light. (Source data are provided as a Source Data file).

445 nm, the crystals afford circular microcrystals with an average curvature (κ, which corresponds to the reciprocal of the radius, $1/R$), of $\kappa = 11$, 12, and 11 mm^{-1}, respectively. With light at 470 nm, although the crystals still exhibited noticeable bending, the delamination was markedly slower, resulting in a reduced average curvature, $\kappa = 5$ mm^{-1}. In contrast, no photomechanical behavior was observed under 515 nm illumination. This observation is clearly related to the solid-state absorption properties of **MBID** (Fig. 4a), for which the solid-state absorption spectra show that it absorbs strongly at 365 nm, 405 nm, and 445 nm, while the absorption is lower at 470 nm, and the material practically does not absorb at 515 nm. Based on these findings, 405 nm was selected as the illumination wavelength for further investigation of the factors that affect the curvature of the microcrystals.

The nascent **MBID** crystals were exposed to 405 nm light (100 mW) until delamination was initiated, yielding 65 product microcrystals, and the distribution of the curvature of these microcrystals was systematically analyzed (Fig. 4b and Supplementary Fig. 8). The results showed that the maximum curvature was $\kappa = 20$ mm^{-1}, while the minimum was 3 mm^{-1}. Statistical analysis revealed that 13 microcrystals (20.0% of the total) exhibited curvatures in the range $\kappa = 0$–10 mm^{-1}. The majority of microcrystals, 42 in total (64.6%), had curvatures in the range $\kappa = 10$–15 mm^{-1}, while 10 microcrystals (15.4%) had curvatures between $\kappa = 15$–20 mm^{-1}. These results indicate that most microcrystals had curvatures in the range $\kappa = 10$–15 mm^{-1}, demonstrating significant uniformity and controllability. To further validate the controllability of the delamination process, **MBID** crystals were irradiated with a 405 nm light of varying powers until delamination occurred, and the curvature distribution of the resulting microcrystals was analyzed (Fig. 4c). At an excitation power of 12 mW, 8 microcrystals (80.0% of the total) exhibited curvatures in the range of $0 < \kappa < 10$ mm^{-1}, while 2 microcrystals (20.0%) displayed curvatures in the range of $10 < \kappa < 20$ mm^{-1}. As the excitation power increased, the number of microcrystals with curvatures of $0 < \kappa < 10$ mm^{-1} gradually decreased, while those with curvatures of $10 < \kappa < 20$ mm^{-1} progressively increased. At an excitation power of 150 mW, only one microcrystal (6.3%) had a curvature of $0 < \kappa < 10$ mm^{-1}, whereas 15 microcrystals (93.7%) exhibited curvatures in the range of $10 < \kappa < 20$ mm^{-1}. These findings suggest that increased excitation power enhances the formation of more strongly curled microcrystals.

Further, we investigated the effect of thickness of the parent **MBID** crystal on the curvature of the resulting microcrystals (Fig. 4d). Our experimental data showed that when the crystal thickness is 10 μm, only microcrystals with curvatures $10 < \kappa < 20$ mm^{-1} are obtained, with a total of 11 microcrystals accounting for 100% of the population. As the crystal height increases, the number of microcrystals with curvatures of $10 < \kappa < 20$ mm^{-1} gradually decreases, while those with curvatures $0 < \kappa < 10$ mm^{-1} progressively increase. When the crystal thickness reaches 42 μm, the number of microcrystals with curvatures of $0 < \kappa < 10$ mm^{-1} rises significantly to 10 (83.3% of the total), whereas those with curvatures of $10 < \kappa < 20$ mm^{-1} decrease to 2 (16.7% of the total). These results clearly show that thinner parent crystals are more likely to produce strongly curled microcrystals, while thicker crystals tend to generate less curved ones. Further statistical

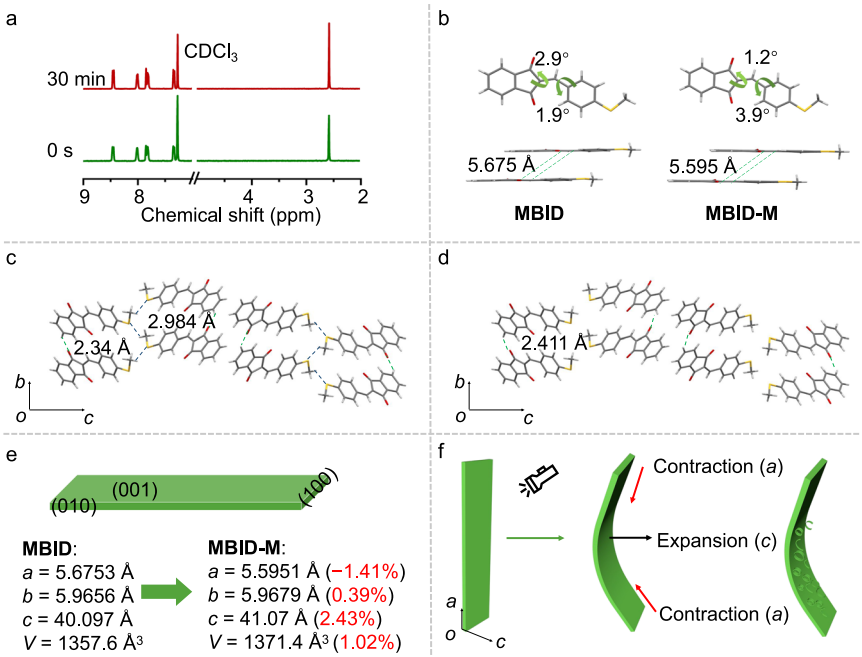

Fig. 5 | Structural changes that drive the delamination and curling. a ^{1}H NMR spectrum of **MBID** crystals before and after irradiation by 365 nm light for 30 min (400 MHz, $CDCl_3$). **b** The dihedral angles between the plane of the double bond and the planes of the two benzene rings, and the distance between the double bonds of two parallel molecules. **c**, **d** Intermolecular interactions in **MBID** (**c**) and **MBID-M** (**d**) along the *a* axis. **e** Schematic diagram showing the face indices of a typical **MBID** crystal before irradiation, and cell parameters of **MBID** and **MBID-M.** **f** Schematic illustration of photoinduced bending and delamination of a crystal of **MBID**.

analysis returned a significant correlation between the thickness of microcrystals and their curvature (Fig. 4e). When the microcrystal thickness is less than 4 μm, the curvature exhibits a broad distribution ranging $\kappa = 9–18\ mm^{-1}$, with an average curvature $\kappa_{ave} = 13.58\ mm^{-1}$. As the thickness increases, the curvature decreases progressively. For microcrystals with a thickness of 16 to 20 μm, the curvature range narrows significantly, to $\kappa = 4–8\ mm^{-1}$, and the average curvature decreases to $\kappa_{ave} = 6.17\ mm^{-1}$. These observations clearly indicate that there is a strong negative correlation between the microcrystal thickness and the curvature, with the thicker microcrystals exhibiting lower curvatures.

To further enhance the curvature of microcrystals, we trialed extended illumination following the delamination. However, the experimental results revealed that prolonged exposure did not only fail to increase the curvature, but instead it caused a significant reduction. When illumination was halted immediately after delamination, the microcrystals exhibited a curvature distribution $\kappa = 11–20\ mm^{-1}$ (Fig. 4f), with $\kappa_{ave} = 14.03\ mm^{-1}$ (Supplementary Fig. 9). Prolonging the illumination for 10 s reduced the curvature $\kappa = 6–19\ mm^{-1}$ (Fig. 4g) and $\kappa_{ave} = 12.83\ mm^{-1}$ (Supplementary Fig. 9). Extending the illumination to 20 s further narrowed the curvature range to $\kappa = 5–19\ mm^{-1}$ (Fig. 4h) with the average decreasing to $\kappa_{ave} = 8.91\ mm^{-1}$ (Supplementary Fig. 9). This phenomenon may be related to the light-driven bending behavior of crystals in the presence of light. As shown in Supplementary Fig. 10, when a crystal is exposed to light and undergoes delamination, two types of microcrystals can be produced, an arc-shaped microcrystal (type 1) and a quasicircular microcrystal (type 2). We further categorize the arc-shaped microcrystals into type 1a and type 1b, where type 1a and 1b represent the more strongly and slightly curved arc-shaped microcrystals, respectively. When light is continuously, the convex surface of arc-shaped type 1a crystal is exposed to the light due to its greater curvature, and further light irradiation causes its convex side to bend towards the light, resulting in decrease in curvature. Arc-shaped microcrystals, type 1b, are less curved, and both the inner and outer surfaces of the curved surface are exposed to the light, and thus their curvature remains nearly constant. The curvature of the quasi-circular microcrystals remains constant due to the stability of the ring structure. Therefore, when photoinduced delamination occurs, continuous light irradiation results in decreased curvature.

Photomechanical motion mechanism and crystal structure of MBID

The complexity of the observed photomechanical effects compelled us to explore the underlying mechanisms. Initially, we hypothesized that the presence of double bond in the molecular structure might enable a [2 + 2] cycloaddition upon irradiation, similar to some other examples[60]. However, single-crystal X-ray diffraction data of **MBID** crystals revealed that the distance between the double bonds of two parallel molecules is 5.675 Å (Fig. 5b). According to the Schmidt's topochemical rule, this distance exceeds significantly the 4.2 Å threshold required for [2 + 2] cycloaddition in the solid state[61]. Although there have been reports of [2 + 2] cycloaddition occurring in crystal structures that do not strictly adhere to the topochemical criterion for reactivity[62,63], our analytical characterization did not show such behavior. **MBID** crystals were irradiated with 365 nm UV light for 30 min and subsequently analyzed by NMR spectroscopy (Supplementary Fig. 2). The lack of changes in both the NMR spectra (Fig. 5a) and the infrared (IR) spectra (Supplementary Fig. 11) before and after irradiation further confirmed that no detectable photochemical reaction occurs in **MBID** upon exposure to light. In order to exclude the possibility of solvent release during illumination[64] causing the crystal delamination, the sample was analyzed by several techniques. SCXRD (Fig. 5b) did not show any solvent molecules in the crystal lattice. Furthermore, ^{1}H NMR spectroscopy (Supplementary Figs. 1, 2) did not detect solvent peaks from dichloromethane or ethanol in samples grown by slow evaporation from dichloromethane and ethanol, and the water peaks were still detected after 30 min of illumination, suggesting that the signals originated from the deuterated chloroform used for measurement. Thermogravimetric analysis (Supplementary Fig. 12) and differential scanning calorimetry (DSC)

(Supplementary Fig. 4) did not show mass loss or thermal effects in the temperature range 300–400 K, further excluding the possibility of desolvation. The results therefore rule out the possibility that effects due to release of solvent cause the delamination.

To determine whether the photothermal effect drives the photomechanical motion[65,66], infrared thermal imaging was used to monitor the surface temperature distribution of the crystal during irradiation. We used infrared thermography to monitor the dynamic change of the crystal surface temperature under 405 nm laser irradiation (power range: 12–150 mW; temperature rise range: $\Delta T = 4–23$ K), and found that the temperature rise was positively correlated with the laser power, and the temperature quickly returned to the ambient temperature after the irradiation has ceased (Supplementary Fig. 13). Notably, despite the significant photothermal effect of the crystals, DSC analysis did not detect any characteristic peaks of the phase transition in the 290–313 K interval (Supplementary Fig. 4). Furthermore, when the crystal was immersed in an ice-water bath, the photomechanical actuation was still observed (Supplementary Movie 8). These findings exclude contributions to the observed photomechanical behavior from photothermally induced phase transitions and thermal expansion.

Combining computational insights with experimental validation, we aimed to establish a correlation between molecular conformational changes and macroscopic photomechanical responses in **MBID** crystals. Previous studies on significant excited-state torsion of analogous molecules provided critical context for understanding **MBID**'s behavior[67–70]. To relate the molecular-scale dynamics with the macroscopic, crystal-level phenomena, we performed excited-state conformational simulations revealing significant structural reorganization: the dihedral angle between the two benzene ring planes was found to increase from 4.5° in the ground state to 24.5° in the excited state (Supplementary Fig. 14). This pronounced torsional rearrangement likely alters molecular stacking patterns, thereby generating the strain necessary for photomechanical actuation. To test this hypothesis at the crystalline level, we systematically investigated light-induced structural modifications. Microcrystalline **MBID-M** obtained through delamination was irradiated with 405 nm UV light for 1 h to induce significant structural reorganization, and analyzed by SCXRD (Supplementary Table 1).

The crystal structures of **MBID** and **MBID-M** were slightly different. **MBID** and **MBID-M** are in the same crystal system and space group, the orthorhombic space group $P2_12_12_1$. In the structure of **MBID**, the dihedral angles between the plane of the double bond and the planes of the two benzene rings are 2.9° and 1.9°, respectively, with an intermolecular double-bond distance of 5.675 Å between the parallel molecules. In **MBID-M**, the respective dihedral angles are 1.2° and 3.9°, and the intermolecular double-bond distance was reduced to 5.595 Å (Fig. 5b). Face indexing of the crystal by SCXRD (Supplementary Fig. 6) and modelling of the crystal habit (Supplementary Fig. 15) identified the long axis of the **MBID** crystal as the crystallographic *a* direction. Along [010], the adjacent molecules are connected through C − H • • • O hydrogen bonds (H • • • O distance: 2.34 Å), forming columns of stacked molecules. In the [001] direction, adjacent columns are further linked by C − H • • • S interactions (H • • • S distance: 2.984 Å). In contrast, the **MBID-M** crystal exhibits C − H • • • O hydrogen bonds (H • • • O distance: 2.411 Å) only along the [010] direction (Fig. 5c, d). Comparison of the crystal structures of **MBID** and **MBID-M** revealed that after UV irradiation, the crystal undergoes contraction of 1.41% along the *a* axis (from 5.6753 to 5.5951 Å), slight expansion of 0.39% along the *b* axis (from 5.9656 to 5.9679 Å), and expansion of 2.43% along the *c* axis (from 40.097 to 41.07 Å) (Fig. 5e and Supplementary Table 1). The powder XRD pattern of **MBID** after in situ illumination with a 405 nm light for 2 min showed new peaks, which correspond to peaks in the powder XRD pattern simulated from the single crystal XRD data of **MBID-M**. This confirms the structural transformation of the crystal from **MBID** to **MBID-M** upon illumination (Supplementary Fig. 16).

Figure 5f summarizes the mechanism suggested for photoinduced delamination and provides a viable explanation for the observations (Fig. 5f). Upon exposure to light, the **MBID** structure undergoes a transformation that results in a change of the **MBID** packing to that of **MBID-M**. According to the SCXRD data, the *a* axis contracts by 1.41% (from 5.67 Å to 5.59 Å) after light irradiation, resulting in photoinduced bending toward the light source. The *c* axis expands by 2.43% (from 40.10 Å to 41.07 Å) after exposure (Fig. 5e), and this anisotropic expansion results in accumulation of strain inside the crystal. The elastic energy gradually accumulates as the ratio of **MBID-M** increases with prolonged light exposure. When the accumulated strain eventually exceeds the energy of the C − H • • • S interactions between the neighboring stacked molecular columns, the connections between the molecular columns break, leading to the photoinduced delamination. If the induction of this process is short, the strain is accumulated rapidly and results in formation of a microcrack, which leads to fracture, and ultimately manifests as the photosalient effect.

Potential applications of quasicircular crystals

The formation of the circular microcrystal through photoinduced delamination produces an optical environment distinct from that of the original flat crystal. To further investigate the optical properties, we performed microregion fluorescence spectroscopy analysis using laser confocal microscopy, and compared the optical behavior of the original crystal and the hollow circular microcrystal. Specifically, we employed the spectral mode of confocal microscopy to obtain fluorescence intensity images of the original crystal and the circular microcrystal under 488 nm laser excitation. The fluorescence intensity variations at different distances from the edges of both crystals were analyzed at the maximum emission peak (527 nm). It was first confirmed that the background signal was about 50. As shown in Fig. 6, microregion fluorescence spectroscopy analysis using laser confocal microscopy revealed very different optical behavior between the original crystal (Fig. 6a, b) and the circular microcrystal (Fig. 6c, d). In the original crystal, the fluorescence signals were confined within a 3 μm range at the crystal edge (the intensity was ~1.5-times the background), decaying to background levels beyond 4 μm (Fig. 6e). Notably, the circular microcrystal formed through photodelamination exhibited a characteristic optical behavior: significant fluorescence signals were detected not only near the periphery but also at the geometric center (60 μm from the edge in the material-free cavity region), with substantially slower internal signal attenuation rates compared to the external regions (Fig. 6f). Comparative experiments demonstrated that at 10 μm from the edge, the circular microcrystal exhibited 5-fold stronger background fluorescence intensity, whereas the pristine crystal showed no detectable signal at this position (Fig. 6g). This evidence confirms the light-field redistribution capability of these circular microstructures. We suggest that multiple internal reflections and constructive interference within the ring structure result in localized field enhancement. This optical confinement extends the fluorescence signal beyond the near-field region, which is not present in the pristine crystal. This behavior is similar to the Whispering Gallery Mode generation, and suggests potential applications for photonic sensing, especially in remote fluorescence detection[71]. In contrast to planar microstructures, closed geometries allow for excellent light-field manipulation through curvature-induced confinement, which enhances light-matter interaction.

In summary, this study presents an organic crystalline material capable of photoinduced delamination. When exposed to visible and ultraviolet light, the material undergoes a progressive photomechanical process in which the crystals are bent toward the light, followed by photosalience and photoinduced delamination and the formation of arc-shaped and ring-shaped organic microcrystals. These microcrystals preserve the excellent flexibility of the parent crystal and exhibit structural stability, maintaining their ring-shaped morphology even under

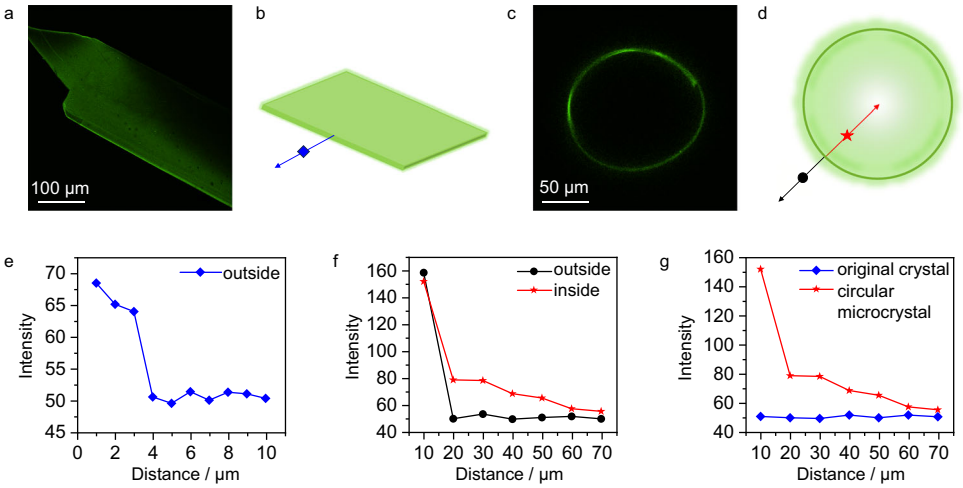

Fig. 6 | Fluorescence characterization of original and circular microcrystals. **a** Fluorescence image of the original crystal captured by confocal microscopy. **b** Schematic diagram of the fluorescence measurement near the edge of the original crystal. **c** Fluorescence image of the circular microcrystal captured by confocal microscopy. **d** Schematic diagram of the fluorescence measurement near the edge of the circular microcrystal. **e** Fluorescence intensity at different distances from the edge of the original crystal. **f** Fluorescence intensity at various positions on the inner and outer sides of the circular microcrystal. **g** Comparison of fluorescence intensities at corresponding distances from the original crystal and the circular microcrystal. (Source data are provided as a Source Data file).

external mechanical forces. Through a systematic investigation of the key factors influencing the photoinduced delamination process, the controllability of this technique was successfully demonstrated, enabling the precise fabrication of arc-shaped and ring-shaped microcrystals. Additionally, crystal structure analysis provided a plausible explanation for this phenomenon, linking it to structural changes in the crystal. Notably, the circular microcrystals exhibit distinct optical properties, including fluorescence signals at both the periphery and the geometric center, attributed to multiple internal reflections and constructive interference. This study not only highlights the potential of photoinduced delamination for producing microcrystals with unconventional morphologies but also reveals that ring-shaped organic microcrystals exhibit intriguing structural properties and exceptional flexibility. These characteristics make them promising candidates for applications in optical devices, sensors, and stimuli-responsive materials, laying a solid foundation for the design and development of flexible, organic, crystalline functional materials.

Methods

Synthetic procedure for MBID

All reagents employed in the syntheses were procured from commercial sources. Analytical-grade solvents were used as received, without any further purification. For the synthesis (Supplementary Fig. 17), 1*H*-indene-1,3(2*H*)-dione (96.54%) (1.46 g, 10 mmol) and 4-(methylthio)benzaldehyde (98%) (1.52 g, 10 mmol) was dissolved in ethanol (50 mL) and NaOH (0.8 mg, 0.2 mmol) was added. The mixture was stirred at room temperature for 6 h and filtered. The filter cake was dried and purified by column chromatography (silica gel, 1:1 petroleum ether/dichloromethane) to provide the compound (**MBID**) as a yellowish green solid (2.35 g, 84%). ^{1}H NMR (400 MHz, chloroform-*d*) δ 8.45 (d, *J* = 8.2 Hz, 2H), 8.01 (s, 2H), 7.85 (s, 1H), 7.82 (s, 2H), 7.33 (d, *J* = 8.2 Hz, 2H), 2.57 (s, 3H). ^{13}C NMR (101 MHz, chloroform-*d*) δ 190.44, 189.21, 147.18, 146.26, 142.43, 139.95, 135.19, 134.99, 134.69, 129.52, 127.82, 124.92, 123.17, 123.14, 14.61.

Characterization

The ^{1}H and ^{13}C{^{1}H} NMR spectra were recorded on an Agar Scientifica 400 MHz spectrometer, with tetramethylsilane as an internal standard. UV–vis absorption spectra were recorded using a Shimadzu UV-2550 spectrophotometer. The emission spectra of crystals were recorded using an Ocean Optics Maya2000 Pro CCD spectrometer or a Shimadzu RF-5301 spectrometer. The mechanical tests were carried out on an Instron 5944 universal materials tester with a 5 N Instron 2530 load cell. Differential scanning calorimetric (DSC) analysis was conducted using a TA Instruments DSC Q20 calorimeter, operating under a nitrogen atmosphere with a heating rate of 10 K/min. The scanning electron microscopy (SEM) images were recorded using FEI Quanta 450 microscope operated at 3 kV. The IR spectra were recorded with a Bruker Vertex 80v FTIR spectrometer. After rcording the IR spectra of **MBID**, the crystals were illuminated in situ for 30 min and the spectrum was recorded again.

X-ray crystallographic analysis

Powder X-ray diffraction (PXRD) data was collected on a Rigaku SmartLab diffractometer with CuK_α radiation. Single crystal X-ray diffraction data were collected using a Bruker D8 Quest diffractometer (CuK_α, λ = 1.54178 Å). Indexing and data integration were performed using APEX4 (Difference Vectors method)[72]. Absorption correction was applied by the multiscan method implemented in SADABS[73]. The structures were solved using SHELXL-2014 (direct methods) and refined using SHELXL-2014 (full-matrix least-squares on F^2) with anisotropic displacement parameters and using the APEX4 program packages. Hydrogen atoms on carbon and nitrogen were placed at ideal positions with their isotropic displacement parameters set to 1.2 × U_{eq} of the atoms to which they are bonded.

Crystal growth

0.6 g of **MBID** powder was dissolved in 100 mL of CH_2Cl_2 to prepare a dilute solution (21 mmol/L). 6 mL of this solution was transferred into a test tube, and an equal volume of ethanol was carefully added along the inner wall of the test tube, ensuring that the two phases remain separated. The test tube was closed with cotton and placed in the dark at room temperature. **MBID** crystals were obtained after about ten days.

Data availability

The crystallographic information has been deposited at the Cambridge Crystallographic Data Centre (CCDC). The CCDC deposition number for **MBID** is 2404489 and for **MBID-M** is 2404490. These data can be obtained free of charge from The Cambridge Crystallographic Data Centre via www.ccdc.cam.ac.uk/data_request/cif. All data are available from the corresponding authors upon request. Source data are provided with this paper.

References

1. Naumov, P. et al. The rise of the dynamic crystals. *J. Am. Chem. Soc.* **142**, 13256–13272 (2020).
2. Dai, S. et al. Strategies to diversification of the mechanical properties of organic crystals. *Angew. Chem. Int. Ed.* **63**, e202320223 (2024).
3. Awad, W. M. et al. Mechanical properties and peculiarities of molecular crystals. *Chem. Soc. Rev.* **52**, 3098–3169 (2023).
4. Zhao, Z. et al. Photochromic luminescence of organic crystals arising from subtle molecular rearrangement. *Nat. Commun.* **15**, 5054 (2024).
5. Chinnasamy, R. et al. Pressure and temperature induced dual responsive molecular crystals: effect of polymorphism. *Cryst. Growth Des.* **22**, 615–624 (2022).
6. Liu, Y. et al. Bioinspired soft robots based on the moisture-responsive graphene oxide. *Adv. Sci.* **8**, 2002464 (2021).
7. Wu, W. et al. Stimuli-responsive flexible organic crystals. *J. Mater. Chem. C* **11**, 2026–2052 (2023).
8. Mondal, S. et al. Autonomous self-healing organic crystals for nonlinear optics. *Nat. Commun.* **14**, 6589 (2023).
9. Lv, Z., Lv, Q., Feng, T., Jiang, J. & Wang, X. Epitaxial growth of two-dimensional organic crystals with in-plane heterostructured domain regulation. *J. Am. Chem. Soc.* **146**, 25755–25763 (2024).
10. Al-Kaysi, R. O. & Bardeen, C. J. General method for the synthesis of crystalline organic nanorods using porous alumina templates. *Chem. Commun.* **21**, 1224–1226 (2006).
11. Yang, X., Al-Handawi, M. B., Li, L., Naumov, P. & Zhang, H. Hybrid and composite materials of organic crystals. *Chem. Sci.* **15**, 2684–2696 (2024).
12. Wang, Y., Shang, H., Li, B. & Jiang, S. Reversible luminescence "off–on" regulation based on tunable photodimerization via crystal-to-cocrystal transformation. *J. Mater. Chem. C* **10**, 734–741 (2022).
13. Qi, H. et al. Hybrid strategies for enhancing the multifunctionality of smart dynamic molecular crystal materials. *Chem. Eur. J.* **31**, e202403293 (2025).
14. Hui, Z. et al. Green flexible electronics: natural materials, fabrication, and applications. *Adv. Mater.* **35**, 2211202 (2023).
15. Wei, C. et al. Flexible molecular crystals for optoelectronic applications. *Chem. Soc. Rev.* **53**, 3687–3713 (2024).
16. Morimoto, T. et al. Ring-shaped Re(I) multinuclear complexes with unique photofunctional properties. *J. Am. Chem. Soc.* **135**, 13266–13269 (2013).
17. Chen, Y., Jing, B., Chang, Z. & Gong, J. Luminescent möbius strip of a flexible halogen-bonded cocrystal evolved from ring and helix. *Jacs Au* **2**, 2686–2692 (2022).
18. Kamachi, M. et al. Synthesis of a gold–silver alloy nanocluster within a ring-shaped polyoxometalate and its photocatalytic property. *Angew. Chem. Int. Ed.* **63**, e202408358 (2024).
19. Guo, J. et al. Crown ethers in graphene. *Nat. Commun.* **5**, 5389 (2014).
20. Winkler, H. D. F., Dzyuba, E. V., Springer, A., Losensky, L. & Schalley, C. A. Gas-phase organocatalysis with crown ethers. *Chem. Sci.* **3**, 1111–1120 (2012).
21. Jin, H., Yang, L., Ahonen, M. J. R. & Schoenfisch, M. H. Nitric oxide-releasing cyclodextrins. *J. Am. Chem. Soc.* **140**, 14178–14184 (2018).
22. Yang, Y. et al. Atomic-level molybdenum oxide nanorings with full-spectrum absorption and photoresponsive properties. *Nat. Commun.* **8**, 1559 (2017).
23. Zhang, M. et al. Broadband electro-optic frequency comb generation in a lithium niobate microring resonator. *Nature* **568**, 373–377 (2019).
24. Liu, W. et al. An integrated parity-time symmetric wavelength-tunable single-mode microring laser. *Nat. Commun.* **8**, 15389 (2017).
25. Al-Kaysi, R. O., Müller, A. M., Frisbee, R. J. & Bardeen, C. J. Formation of cocrystal nanorods by solid-state reaction of tetracyanobenzene in 9-methylanthracene molecular crystal nanorods. *Cryst. Growth Des.* **9**, 1780–1785 (2009).
26. Al-Kaysi, R. O., Müller, A. M. & Bardeen, C. J. Photochemically driven shape changes of crystalline organic nanorods. *J. Am. Chem. Soc.* **128**, 15938–15939 (2006).
27. Kim, T., Zhu, L., Mueller, L. J. & Bardeen, C. J. Mechanism of photoinduced bending and twisting in crystalline microneedles and microribbons composed of 9-methylanthracene. *J. Am. Chem. Soc.* **136**, 6617–6625 (2014).
28. Cao, C. et al. Photodimerization-triggered photopolymerization of triene coordination polymers enables macroscopic photomechanical movements. *J. Am. Chem. Soc.* **146**, 25028–25034 (2024).
29. Tahir, I. et al. Photomechanical crystals as light-activated organic soft microrobots. *J. Am. Chem. Soc.* **146**, 30174–30182 (2024).
30. Li, W., Gately, T. J., Kitagawa, D., Al-Kaysi, R. O. & Bardeen, C. J. Photochemical reaction front propagation and control in molecular crystals. *J. Am. Chem. Soc.* **146**, 32757–32765 (2024).
31. Kitagawa, D. et al. Control of photomechanical crystal twisting by illumination direction. *J. Am. Chem. Soc.* **140**, 4208–4212 (2018).
32. Al-Kaysi, R. O. & Bardeen, C. J. Reversible photoinduced shape changes of crystalline organic nanorods. *Adv. Mater.* **19**, 1276–1280 (2007).
33. Rath, B. B. & Vittal, J. J. Mechanical bending and modulation of photoactuation properties in a one-dimensional Pb(II) coordination polymer. *Chem. Mater.* **33**, 4621–4627 (2021).
34. Li, P., Ji, C., Liu, M., Müllen, K. & Yin, M. Hydrogen-bonded homochiral molecular crystals with mechanical elasticity and photomechanical bending. *Chem. Mater.* **35**, 4564–4571 (2023).
35. Bushuyev, O. S., Tomberg, A., Friščić, T. & Barrett, C. J. Shaping crystals with light: crystal-to-crystal isomerization and photomechanical effect in fluorinated azobenzenes. *J. Am. Chem. Soc.* **135**, 12556–12559 (2013).
36. Lam, K. et al. Solar-powered molecular crystal motor based on an anthracene–thiazolidinedione photoisomerization reaction. *J. Am. Chem. Soc.* **146**, 18836–18840 (2024).
37. Wei, Y. et al. Photoactuators based on plastically flexible α-cyanostilbene molecular crystals driven by the solid-state [2+2] cycloaddition reaction. *Small* **20**, 2307756 (2024).
38. Dong, X. et al. Effects of template and molecular nanostructure on the performance of organic–inorganic photomechanical actuator membranes. *Adv. Funct. Mater.* **30**, 1902396 (2020).
39. Al-Kaysi, R. O. et al. Chemical reaction method for growing photomechanical organic microcrystals. *CrystEngComm* **17**, 8835–8842 (2015).
40. Al-Kaysi, R. O., Tong, F., Al-Haidar, M., Zhu, L. & Bardeen, C. J. Highly branched photomechanical crystals. *Chem. Commun.* **53**, 2622–2625 (2017).
41. Nag, S., Emmerling, F., Tothadi, S., Bhattacharya, B. & Ghosh, S. Distinct photomechanical responses of two new 1,3-dimethylbarbituric acid derivative crystals. *CrystEngComm* **26**, 2871–2882 (2024).
42. Liu, C. et al. Fast photoactuation of elastic crystals based on 3-(naphthalen-1-yl)-2-phenylacrylonitriles triggered by subtle photoisomerization. *J. Mater. Chem. C* **10**, 14273–14281 (2022).
43. Ghate, P. P. et al. Light-triggered rolling and unrolling of molecular crystal microsheets. *Cryst. Growth Des.* **24**, 7695–7703 (2024).
44. Kim, T., Al-Muhanna, M. K., Al-Suwaidan, S. D., Al-Kaysi, R. O. & Bardeen, C. J. Photoinduced curling of organic molecular crystal nanowires. *Angew. Chem. Int. Ed.* **52**, 6889–6893 (2013).
45. Tong, F., Kitagawa, D., Dong, X., Kobatake, S. & Bardeen, C. J. Photomechanical motion of diarylethene molecular crystal nanowires. *Nanoscale* **10**, 3393–3398 (2018).
46. Zhu, L. et al. Characterization of a P-type photomechanical molecular crystal based on the $E \rightarrow Z$ photoisomerization of 9-divinylanthracene malonitrile. *J. Mater. Chem. C* **4**, 8245–8252 (2016).
47. Zhang, C., Zhang, T., Li, T., Xu, T. & Tong, F. Turning on photomechanical responses in molecular crystals of anthracenyl thiazole derivatives by regulating intermolecular interactions. *Cryst. Growth Des.* **24**, 193–204 (2024).

48. Zhu, L., Al-Kaysi, R. O. & Bardeen, C. J. Reversible photoinduced twisting of molecular crystal microribbons. *J. Am. Chem. Soc.* **133**, 12569–12575 (2011).
49. Takanabe, A. et al. Optical activity and optical anisotropy in photomechanical crystals of chiral salicylidenephenylethylamines. *J. Am. Chem. Soc.* **138**, 15066–15077 (2016).
50. Yue, Y. et al. Molecular twisting affects the solid-state photochemical reactions of unsaturated ketones and the photomechanical effects of molecular crystals. *Chem. Eur. J.* **29**, e202203178 (2023).
51. Li, P., Guan, J., Peng, M., Wu, J. & Yin, M. Spontaneous and photomechanical twisting of a cyanostilbene-based molecular crystal. *J. Mater. Chem. C* **11**, 8564–8569 (2023).
52. Peng, C. et al. Diverse macroscopic helical motions of microribbons driven by electrons. *Chem. Commun.* **53**, 2578–2581 (2017).
53. Tamaoki, M., Kitagawa, D. & Kobatake, S. Light-driven rapid peeling of photochromic diarylethene single crystals. *Cryst. Growth Des.* **21**, 3093–3099 (2021).
54. Nakagawa, Y., Morimoto, M., Yokojima, S., Nakamura, S. & Uchida, K. Efficient surface peeling, a photoinduced result of photochromic diarylethene crystal by multistep light irradiation. *Cryst. Growth Des.* **23**, 1581–1591 (2023).
55. Kurakula, U. et al. Photoreactive Zn(II) coordination compounds: exploring biomimetic mechanical motion and photosalient behavior. *Cryst. Growth Des.* **24**, 7066–7074 (2024).
56. Tong, F., Al-Haidar, M., Zhu, L., Al-Kaysi, R. O. & Bardeen, C. J. Photoinduced peeling of molecular crystals. *Chem. Commun.* **55**, 3709–3712 (2019).
57. Lin, J. et al. Highly efficient *in crystallo* energy transduction of light to work. *Nat. Commun.* **15**, 3633 (2024).
58. Wang, Y., Zhang, Q., Liu, Q., Abrahams, B. F. & Lang, J. The use of photocycloaddition reactions to drive mechanical motions resembling humanoid movements. *Angew. Chem. Int. Ed.* **63**, e202409472 (2024).
59. Naumov, P., Sahoo, S. C., Zakharov, B. A. & Boldyreva, E. V. Dynamic single crystals: kinematic analysis of photoinduced crystal jumping (the photosalient effect). *Angew. Chem. Int. Ed.* **52**, 9990–9995 (2013).
60. Naumov, P. et al. Topochemistry and photomechanical effects in crystals of green fluorescent protein-like chromophores: effects of hydrogen bonding and crystal packing. *J. Am. Chem. Soc.* **132**, 5845–5857 (2010).
61. Schmidt, G. M. J. Photodimerization in the solid state. *Pure Appl. Chem.* **27**, 647–678 (1971).
62. Yadava, K. & Vittal, J. J. Photosalient behavior of photoreactive Zn(II) complexes. *Cryst. Growth Des.* **19**, 2542–2547 (2019).
63. Nagarathinam, M., Peedikakkal, A. M. P. & Vittal, J. J. Stacking of double bonds for photochemical [2+2] cycloaddition reactions in the solid state. *Chem. Commun.* **42**, 5277–5288 (2008).
64. Borchers, T. H. et al. Three-in-one: dye-volatile cocrystals exhibiting intensity-dependent photochromic, photomechanical, and photocarving response. *J. Am. Chem. Soc.* **145**, 24636–24647 (2023).
65. Hasebe, S. et al. Photothermally driven high-speed crystal actuation and its simulation. *J. Am. Chem. Soc.* **143**, 8866–8877 (2021).
66. Hasebe, S., Hagiwara, Y., Ueno, T., Asahi, T. & Koshima, H. Negative to positive axial thermal expansion switching of an organic crystal: contribution to multistep photoactuation. *Chem. Sci.* **15**, 1088–1097 (2024).
67. Clark, A. E., Qin, C. & Li, A. D. Q. Beyond exciton theory: a time-dependent DFT and Franck–Condon study of perylene diimide and its chromophoric dimer. *J. Am. Chem. Soc.* **129**, 7586–7595 (2007).
68. Jursenas, S. et al. Free and self-trapped charge-transfer excitons in crystals of dipolar molecules of *N,N*-dimethylaminobenzylidene 1,3-indandione. *J. Phys. Chem. B* **102**, 1086–1094 (1998).
69. Gulbinas, V. et al. Charge transfer induced excited state twisting of *N,N*-dimethylaminobenzylidene-1,3-indandione in solution. *J. Phys. Chem. A* **103**, 3969–3980 (1999).
70. Zhang, Y. et al. Giant morphological change in layered microribbons featuring reversible sliding of stacking layers. *Adv. Mater.* **27**, 320–325 (2015).
71. Yang, S., Wang, Y. & Sun, H. Advances and prospects for whispering gallery mode microcavities. *Adv. Opt. Mater.* **3**, 1136–1162 (2015).
72. Sheldrick, G. M. SHELXT – Integrated space-group and crystal-structure determination. *Acta Cryst. A* **71**, 3–8 (2015).
73. Sheldrick, G. M. A short history of SHELX. *Acta Cryst. A* **64**, 112–122 (2008).

Acknowledgements

This work received support from the National Natural Science Foundation of China (52373181, 52173164), the Natural Science Foundation of Jilin Province (20230101038JC), and funding from New York University Abu Dhabi (AD073). Additionally, this material is based on works supported by Tamkeen under NYUAD RRC Grant No. CG011.

Author contributions

C.D. and B.T. performed the experiments. L.Li, P.N., and H.Z. supervised the experiments. H.Z. and P.N. co-wrote the manuscript.

Competing interests

The authors declare no competing interests.

Additional information

Supplementary information The online version contains supplementary material available at https://doi.org/10.1038/s41467-025-59670-w.

Correspondence and requests for materials should be addressed to Panče Naumov or Hongyu Zhang.

Peer review information *Nature Communications* thanks Meizhen Yin and the other, anonymous, reviewers for their contribution to the peer review of this work. A peer review file is available.